




Mapping the Dynamics of the South Asian Monsoon Using CYGNSS's Level-1 Signal Coherency

Mohammad M. Al-Khaldi , *Member, IEEE*, Rashmi Shah , *Senior Member, IEEE*, Clara C. Chew, *Member, IEEE*, Joel T. Johnson , *Fellow, IEEE*, and Scott Gleason, *Senior Member, IEEE*

Abstract—A method for mapping the dynamics of the South Asian monsoon season is proposed based on the use of the coherence of CYGNSS Level 1 delay-Doppler Map measurements. Because the apparent coherence of the specular forward scattering observed by CYGNSS provides information on the presence of inland water, it can be related to different phases of the monsoon season. Results reported from 2017 to 2020 illustrate inter-annual variations in the seasonal monsoon, and show high degrees of correlation with SMAP soil moisture maps over the Indian subcontinent. Comparisons with precipitation information from the global precipitation measurement mission also show relationships indicative of the monsoon's dry and wet phases. The analysis presented in this work highlights the potential of using spaceborne GNSS-R systems for the operational mapping of monsoon dynamics.

Index Terms—Bistatic radar systems, coherency, cyclone global navigation satellite system (CYGNSS), global navigation satellite systems reflectometry (GNSS-R), inland water dynamics, rough surface scattering.

I. INTRODUCTION

THE South Asian monsoon appears as a seasonal pattern of extended periods of drought and several months of torrential rainfall. The implications this process has on agricultural productivity, food security, sudden flooding and disaster preparedness are of particular importance [1]–[6]. Owing to the vastness of the regions it affects (an area greater than 4 million km²) within the Indian subcontinent extending from approximately 5° N 63.5° E to 32.5° N 99.5° E, spaceborne remote sensing provides an important tool for monitoring the monsoon's development, effects and for acquiring observations to support its prediction [7]–[9].

The properties of the cyclone global navigation satellite system (CYGNSS) mission make it well poised to address this

need. CYGNSS's L-band frequency makes its measurements of surface specular scattering insensitive to cloud cover and to the heavy rain rates that often accompany the monsoon's wet phase. Further, its fine temporal sampling (mean and median revisit times of 7 and 3 h, respectively, for latitudes within $\pm 38^\circ$ [10], [11]) provides an opportunity to map monsoon dynamics at revisit rates as short as 1 d.

This article presents a method for mapping monsoon dynamics over the Indian subcontinent through the use of the coherence of CYGNSS's Level 1 delay Doppler maps (DDMs) [13]. The method is shown to mark the start, end, and evolution of the monsoon's characteristic phases. The results demonstrate the potential for using spaceborne GNSS-R systems in an operational capacity in the mapping of large scale weather phenomena.

The next section provides an overview of the fundamental circulation mechanisms that give rise to the South Asian monsoon, including the basic properties of its “dry” and “wet” phases. It also provides an overview of the CYGNSS mission, the measurements it provides, and the physical mechanisms underlying their sensitivity to various stages of the monsoon. Section III then describes the proposed dynamic monsoon mapping method. Section IV extends the proposed method to the available record of CYGNSS Level-1 data, and illustrates the method's ability to detect and map different cycles of the monsoon. Qualitative and quantitative assessments are also performed through comparisons with soil moisture and precipitation datasets provided by other sensors. Potential limitations of the method are discussed in Section IV, and recommendations for future work and final conclusions are provided in Section V.

II. BACKGROUND

A. Description of the Monsoon Season

The South Asian (Indian) monsoon is caused by interactions between near surface ocean air, varied levels of atmospheric moisture content, and impinging solar radiation. As sunlight heats the ocean's surface near the equator, evaporated water mixes with warmed air creating a flow of wind propagating northwards. The transfer of this large mass of warm moist air creates a region of low pressure with dry air known as the intertropical convergence zone (ITCZ) [14]. This stage of the solar-surface interaction brings about the dry stage of the monsoon season characterized by an absence of rainfall and arid conditions throughout the Indian subcontinent predominately affecting Pakistan, India, Nepal, Bhutan, Bangladesh, Sri-Lanka,

Manuscript received October 22, 2020; revised November 28, 2020; accepted November 30, 2020. Date of publication December 3, 2020; date of current version January 6, 2021. This work was supported in part by an allocation of computing resources from the Ohio Supercomputer Center. (*Corresponding author: Mohammad M. Al-Khaldi.*)

Mohammad M. Al-Khaldi, Clara C. Chew, and Scott Gleason are with the Constellation Observing System for Meteorology, Ionosphere, and Climate (COSMIC) Program, University Corporation for Atmospheric Research (UCAR), Boulder, CO 80301 USA (e-mail: malkhaldi@ucar.edu; clarac@ucar.edu; gleason@ucar.edu).

Joel T. Johnson is with the Department of Electrical and Computer Engineering and ElectroScience Laboratory, The Ohio State University, Columbus, OH 43210 USA (e-mail: johnson.1374@osu.edu).

Rashmi Shah is with Jet Propulsion Laboratory, California Institute of Technology, Pasadena, CA 91109 USA (e-mail: Rashmi.Shah@jpl.nasa.gov).

Digital Object Identifier 10.1109/JSTARS.2020.3042170

and Myanmar. The drought phase typically prevails for a total of 8 mo starting from October and ending in May [14]. As the warmed, humid air reaches its greatest Northward extent, it cools and begins its descent towards the subtropics, where a process of condensation ensues. This marks the beginning of the wet phase and brings about heavy rainfall culminating in transient flooding and inundation over different parts of the Indian subcontinent. The wet phase typically lasts for a period of 4–5 mo from June to early October [14]. This cyclical atmospheric circulation, the Hadley Circulation [15], is the fundamental driver for the monsoon season.

During the dry phase, water resource management, improved water conservation, and distribution practices, and the monitoring of agricultural productivity all are crucial and can have profound implications for food security [1]–[6], [14]. Tracking wet phase dynamics is of particular importance for disaster preparedness due to the heavy and sustained rainfall that can cause flooding, loss of life, and destruction of property [5], [6]. The ability to predict and monitor monsoon dynamics is complicated by its sudden onset and the linkage of its underlying circulation mechanisms, the Hadley Circulation, with other larger scale phenomena such as the El Nino and Southern oscillation (ENSO) phenomenon [14]. As a result, the prediction of monsoon onset and evolution remains challenging with current models [16], [17], motivating exploring the use of remote sensing systems like the CYGNSS constellation.

B. CYGNSS Mission

The CYGNSS mission operates an eight satellite constellation using a mode of remote sensing known as global navigation satellite system-reflectometry (GNSS-R) [10], [11]. Each CYGNSS satellite hosts a GNSS-R payload that receives L-band transmissions from global positioning system (GPS) satellites that have been specularly scattered from Earth's surface.

The received scattered fields arise from a variety of locations including the specular point and the surface surrounding it known as the glistening zone [12], resulting in a diversity of forward scattered contributions. Each contribution occurs at a distinct delay (τ) relative to the specular point. Due to the relative motions between the CYGNSS receiver(s), GPS transmitter(s), and the Earth's surface, the observed forward scatter contributions also occur at different Doppler shifts (f_D). Based on the intersections of ellipses of constant delay and hyperbolas of constant Doppler shifts projected onto Earth's surface, a mapping occurs from Earth's surface into delay-Doppler space, giving rise to the fundamental GNSS-R measurement, the delay-Doppler Map (DDM) [12]. For CYGNSS, the mapping is done by each of the receivers' delay-Doppler mapping instrument [18] payload into a "Full DDM" comprised of 128 delay bins (at $\approx 0.25 \mu s$ sampling) and 20 Doppler bins (at ≈ 500 Hz sampling). About the Full DDM's peak amplitude representing the specular point on the surface, a smaller 17×11 delay-Doppler cropping window is used to form, compress and downlink the standard Level-1 DDM product. Motivated by its global availability (in contrast to other less frequent special CYGNSS modes of operation), this work uses only CYGNSS's standard Level-1

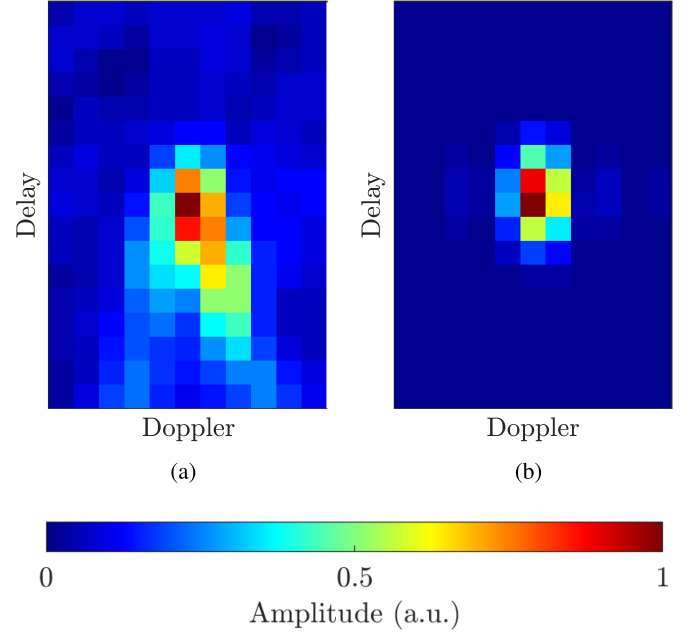


Fig. 1. Illustration of CYGNSS Level-1 DDMs. (a) Dominated by noncoherent scatter. (b) Dominated by coherent reflection.

DDM products. Examples of Level-1 DDMs are depicted in Fig. 1.

C. Sensitivity to Transient Flooding and Inundation

Numerous previous studies have explored the use of radiometers [19], [20], synthetic aperture radars [21], [22], and optical [23] systems for examining monsoon effects. In microwave radiometry, the flooding and inundation effects associated with the monsoon wet phase can cause a decrease in brightness temperatures that can provide indications of monsoon dynamics [19]. In contrast, studies analyzing SAR backscattered normalized radar cross section for vegetated land surfaces have modeled received signals as [24], [25], the sum of three mechanisms describing the aggregated contributions of surface, volume, and surface-to-volume scatter. Through varied interactions between the three fundamental contributions, flooding, and inundation may increase or decrease backscatter levels depending on surface roughness and vegetation conditions. For CYGNSS, one sensitivity to inundation occurs due to direct proportionality of peak received DDM power to surface reflectivity [26], [27]

$$\Gamma_{LR}(\epsilon_s, \theta_i) = \left| \frac{1}{2} (\Re_{VV} - \Re_{HH}) \right|^2 \quad (1)$$

with

$$\Re_{VV} = \frac{\epsilon_s \cos \theta_i - \sqrt{\epsilon_s - \sin^2 \theta}}{\epsilon_s \cos \theta_i + \sqrt{\epsilon_s - \sin^2 \theta}} \quad (2)$$

$$\Re_{HH} = \frac{\cos \theta_i - \sqrt{\epsilon_s - \sin^2 \theta}}{\cos \theta_i + \sqrt{\epsilon_s - \sin^2 \theta}}. \quad (3)$$

Here $\Gamma_{LR}(\epsilon_s, \theta_i)$ is the surface's Fresnel reflectivity in polarization LR (right hand circular incidence and left hand circular

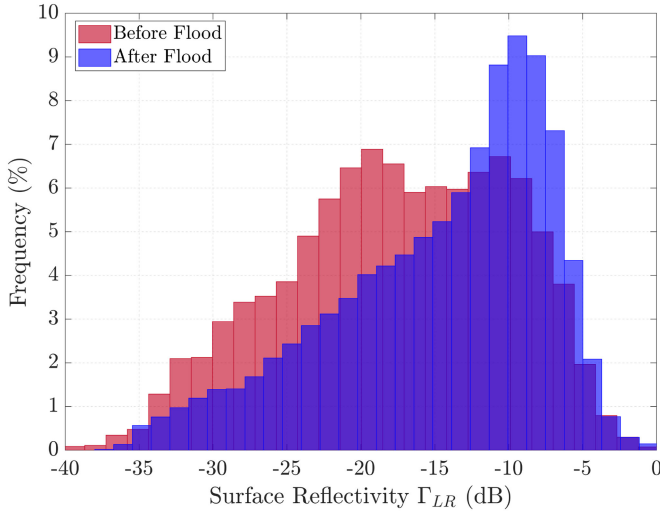


Fig. 2. Changes in CYGNSS surface reflectivity in response to flooding in the vicinity of the Indus river coinciding with the monsoon wet phase.

TABLE I

SUMMARY OF RELEVANT STATISTICS FOR CASE STUDY ILLUSTRATING THE SENSITIVITY OF CYGNSS MEASUREMENT SURFACE REFLECTIVITY TO FLOODING EVENT DETECTED BY MODIS NRT IN THE BASIN ON THE INDUS RIVER, PAKISTAN

	Before Flood	After/During Flood
Start Date	July 1st, 2019	August 1st, 2019
End Date	July 31st, 2019	August 31st, 2019
Number of Measurements	33,069	29,550
Mean Γ_{LR} (dB)	-17.59	-14.59
Std Γ_{LR} (dB)	7.63	7.27
Peak Flood Level (%)	0.00	> 50
Mean NDVI	0.06	0.11
Std NDVI	0.05	0.09

scattering for CYGNSS) and is a function of the surface relative complex permittivity ϵ_s . For land surfaces, ϵ_s depends strongly on the volumetric soil moisture content of the soil [28], [29]. As the monsoon's wet phase begins, increased levels of rainfall cause a significant increase in moisture content. Surface reflectivity therefore undergoes seasonal variations, experiencing increases during flooding and inundation events and a steady decline as volumetric moisture content diminishes during the monsoon's dry phase [30]–[35].

The sensitivity of CYGNSS measurements to these effects is illustrated in Fig. 2, where the surface reflectivity derived from calibrated CYGNSS Level-1 DDMs (corrected for instrument and geometry related parameters) is depicted for one month periods before (July 2019) and after (August 2019) a monsoon related flooding event in the vicinity of the Indus River took place. Table I summarizes properties of these measurements and includes information on the normalized difference vegetation index (NDVI) derived from advanced very high resolution radiometer (AVHRR) observations. The modest changes in NDVI show that other properties of the scene remains similar over the July–August 2019 period. Within the same area, the moderate resolution imaging spectroradiometer (MODIS) near real time

(NRT) suggests that over the month of August, flood occurrence exceeded 50% within the test region. The occurrence percentage is determined based on the portion of MODIS measurements associated with the detection of water relative to total measurements made, with flood state declared based on the number of water observations exceeding “normal” water levels for a given region based on yearly MODIS water masks. The reported flooding event is expected to be the primary driver for the observed 17.06% in mean CYGNSS surface reflectivity after the flooding event.

While CYGNSS's sensitivity to inundation, through increases in its measured surface reflectivities, is apparent in Fig. 1, the reliance on signal amplitude alone represents a significant challenge. In particular, signal amplitudes can be affected not only by inundation but also by surface roughness, vegetation, and other properties. Signal amplitudes are also subject to any calibration uncertainties in the CYGNSS Level 1 products. Accordingly, an alternate method is presented in what follows that avoids these limitations.

III. PROPOSED METHOD

Instead of using variations in the magnitude of CYGNSS observables, the proposed method aims to map the dynamics of the South Asian monsoon by detecting the dominant scattering mechanism of a DDM. The two relevant scattering mechanisms are incoherence and coherence. Incoherent scattering occurs when the received power is scattered from a surface whose height variation is significant compared to the L-band wavelength (19 cm). Due to the random path lengths taken over such a surface, the resulting received surface scatter has a phase that decorrelates rapidly as the satellite moves.

In contrast, coherent scattering occurs when the scattering surface is smooth compared to the wavelength, giving rise to mirror like reflections off the Earth's surface. The resulting scattered fields add constructively, resulting in increased signal amplitudes and a distinct DDM waveform shape [27]. The prevalence of one scattering regime versus another over a given location depends on the level of surface roughness. The studies of [27] and [37] have shown that the roughness scales necessary at the L1 1.575 GHz center frequency are on the order of 3–5 cm or less to support coherence, and the studies of [13] have shown that incoherent scattering occurs for more than 90% of inland returns. For measurements classified as coherent, approximately 80% were found to be associated with the presence of inland water bodies within a measurement's first Fresnel zone. The high correlation between the presence of inland water and the dominance of coherence is the result of the low surface roughness of inland water bodies. For a given location, a transition from incoherence to coherence can result when flooding and inundation occurs. This work therefore aims to apply the recently developed Level-1 detector [13] to detect these transitions and to use them as indicators of monsoon dynamics.

A “power spread” detection method is used in [13] to detect coherence, based on the characteristic waveform shape of coherent scattering which concentrates power within the $\pm 2 \tau$ and $\pm 3 f_D$ region surrounding the DDM peak. This limited

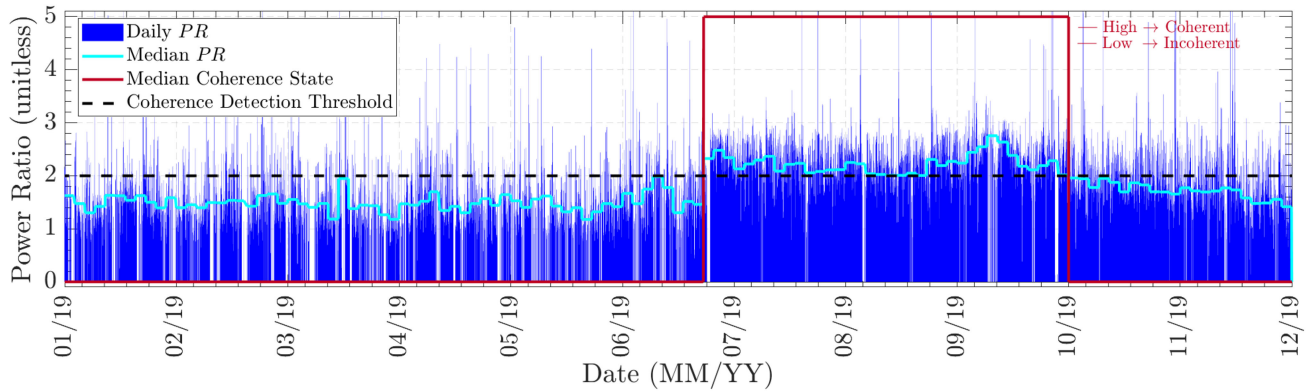


Fig. 3. Level-1 coherence metric for all CYGNSS observations made throughout 2019 for a 36 km footprint centered about 25.76°N 84.09°E. Illustration depicts the transition from a dominant incoherent scattering state during the dry phase of the monsoon to a dominant coherent scattering state during the wet phase of the monsoon.

power spread is captured through a Level-1 coherence metric, the power ratio, that divides the DDM power within this limited region by that within the remainder of the 17×11 larger DDM. For coherent returns, the power ratio is expected to be high. For incoherent returns, there is a greater spread of power within the DDM and the power ratio is low. A globally fixed coherence detection threshold of $PR \geq 2.0$ is recommended as indicative of dominant coherence in [13].

An example is depicted in Fig. 3 for a 36 km grid cell in northern India that includes parts of the Ganges river, Ghaghara river, and Suraha lake as well as drier, rough, terrain within which no known water bodies exist. In contrast to traditional radar systems mapping swaths of the observed surface, using CYGNSS the properties of a given surface may be analyzed through an accumulation of a group of (quasi-random) individual specular points that are not co-located. The power ratio PR is plotted throughout 2019 for all of the nearly 20 000 CYGNSS DDMs (approximately 55 per day on average) falling within this pixel. An increase in the time series measurement density occurs beginning July 1st, 2019 because at this time the CYGNSS mission increased the Level-1 DDM reporting interval from 1 to 2 Hz. The transition was directly in support of land investigations as it reduces along track spatial smearing, particularly for DDMs are dominated by coherent reflection, from a distance of 6 to 3 km.

Depending on the precise location of a DDM specular point within this grid cell, it may be dominated by coherent reflection or incoherent scatter as evidenced by the numerous transitions above/below the 2.0 PR detection threshold in Fig. 3. Therefore, the use of the coherence of a single DDM as an indicator of monsoon effects is expected to give rise to considerable uncertainty. Instead, the dominant mode of scattering within a given grid cell is established based on the median PR value in the grid cell over a longer time period. The latter is indicative of the dominant mode of reflection within a series of measurements for a given location. For days with a daily median power ratio below the detection threshold in Fig. 3, incoherence is declared to be dominant and is taken to indicate a dry phase at this location. A daily median value that exceeds the detection threshold results

in classification in the wet phase. In Fig. 3, the transition to a dominant mode of coherence, ergo the monsoon's wet phase, begins July 9th, and the dry phase transition occurs October 25th, 2019. Note for this location that the daily median PR value remains above or below the 2.0 threshold throughout the entire wet and dry seasons, respectively.

Two limitations exist for the proposed method that require additional consideration. The first relates to the method's focus on observing changes in inundation as an indicator of monsoon properties. Locations within the subcontinent that produce dominant coherence year-round therefore are problematic. For example, 70–90% of Bangladesh's surface experiences a combination of monsoon floods, river bank floods, rain fed floods, and flash floods throughout the year. As a result during both the dry and wet phases of the monsoon, much of Bangladesh is declared coherent. This is further evidenced in the maps in Fig. 4. Therefore this region is excluded from subsequent analysis.

The second limitation relates to the elevation of some of the areas affected by the monsoon. During December 2017, an update was made to all eight CYGNSS receivers to expand the specular search window used on-board the spacecraft in support of land investigations. As a result, the maximum surface elevation for which useful measurements are downlinked expanded to include high altitude regions such as the whole of Nepal and some parts of India and Pakistan. However, the mean 4 km elevation over much of Bhutan renders $\approx 75\%$ of all specular measurements made beyond the minimum permissible delay and as a consequence much of the downlinked measurements over Bhutan are not usable. As a result, Bhutan is excluded from the following studies of this article.

IV. RESULTS AND DISCUSSION

A. Spatial Trends

The dynamics of monsoon induced flooding and inundation are next explored using the multiyear Level-1 data record made available by the CYGNSS mission extending from DOY 77, 2018 to DOY 130, 2020. Fig. 4 plots (a) and (b) depict areas where a dominant mode of coherence is detected before (over

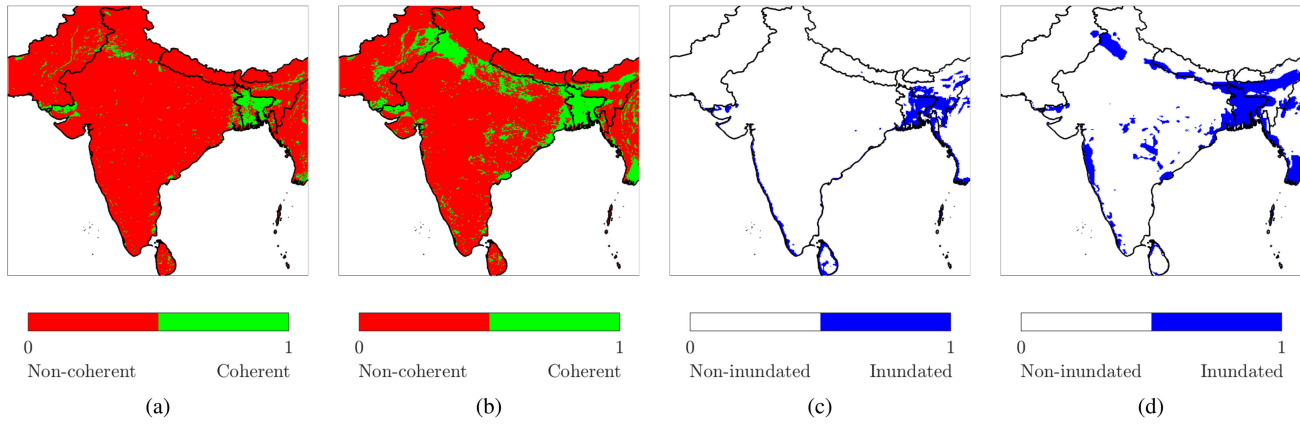


Fig. 4. Illustration of spatial trends associated with dry and wet phases of the monsoon. (a) Distribution of coherent and incoherent points on 9 km grid during dry phase based on 30 d medians throughout May 2018. (b) Distribution of coherent and incoherent points on 9 km grid during the wet phase based on 30 d medians throughout August 2018. (c) Points associated with elevated SMAP soil moistures indicative of inundation on 9 km grid using 30 d mean throughout May 2018. (d) Points associated with elevated SMAP soil moistures indicative of inundation on 9 km grid using 30 d mean throughout August 2018.

May 2018) and after (over July 2018) the onset of the monsoon's wet phase on a 9 km spatial grid using 30 d median PR values. During the dry phase, a total of 5.61% of all grid cells within the Indian subcontinent were associated with coherent reflection. Transient flooding and inundation brought about by the wet phase result in a growth of this percentage to 16.26%.

In the absence of ground truth at comparable spatial and temporal scales, the maps obtained are evaluated using soil moisture measurements from the soil moisture active passive (SMAP) mission on a 9 km grid (the enhanced L2 radiometer half-orbit 9 km EASE-grid soil moisture SPL2MPE product) [40]. Here, a simple approach is applied in which grid pixels having monthly mean moistures that exceed 45% are declared inundated where it is noted that similar thresholding practices have previously been used [41] in the context of agriculture flood mapping with SMAP data; having shown that the upper volumetric soil moisture limit for noninundated soils is $\approx 40\%$ and median sustained volumetric moisture levels during flooding events ranges between $40\% \leq m_v \leq 45\%$. During the dry phase, the SMAP maps in plot (c) suggest that 4.57% of all points are inundated, while a wet phase increase to 12.51% occurs in the plot (d). The qualitative similarity of the resulting images confirms the CYGNSS-based method's capabilities in identifying inundation conditions. Some differences in the two maps arise due to the finer resolution capabilities of CYGNSS at detecting inland waterbodies [45], for example in the border region between Pakistan and India. These detections are associated with known inland water bodies which include the Ramn of Kutch lake, Shakoor lake, Indus river, and Chehab river. To eliminate the contributions of static water bodies, differences between the wet and dry phase maps can be used to estimate the additional area inundated during the monsoon wet phase. In the case of the 2018/2019 cycle depicted in Fig. 4, CYGNSS detects the wet phase resulting in transient flooding and inundation that spans 10.65% of the Indian subcontinent or equivalently 43 110 km² while the reference SMAP dataset suggests that this is 7.94% or equivalently 32 193 km². Again the differences between these

extents likely arise due to the differences in spatial resolution of the water body detections obtained between the two instruments.

Alternatively, to estimate the additional area inundated during the monsoon's wet phase ancillary information [42], [43] pertaining to static inland water body extent could be used to subtract their respective signatures from plot (b). This approach is not used in this work in order to limit the algorithm's dependence on any ancillary information beyond CYGNSS's Level-1 measurements. Another consideration motivating this choice is the fact that the temporal resolutions of a number of reference databases are on the order of > 1 year, appreciably longer than the 1 mo resolution of the CYGNSS products depicted in plots (a)–(b) thereby limiting their ability to capture the dynamic changes a number of the water bodies of interest undergo over the various monsoon phases and their respective intensities.

B. Temporal Trends

While the preceding results highlight the large scale spatial trends associated with the monsoon's characteristic phases, tracking the monsoon's temporal dynamics is also of high interest. Fig. 5 plots the total additional inundated area within India detected by CYGNSS on a 10 d interval and 12 km grid for the 3 a period March 2017 to March 2020. The variations between 0% (dry phase baseline) and $\approx 25\%$ (wet phase maximum) clearly illustrate the monsoon cycle in each year. A number of other recurrent trends are also observed. During the dry phase, the percentage of points detected as being coherent undergoes a near monotonic decrease following the wet phase. This is expected to be the result of prolonged periods of drought resulting in a sustained drying of previously inundated areas. A minimum of $< 1\%$ is typically reached near the end of the dry phase. A subsequent near monotonic increase marks the onset of the wet phase.

The total ten-day rainfall over India obtained from the global precipitation mission (GPM) [44] is also included in Fig. 5. A lag between the onset of elevated precipitation and CYGNSS

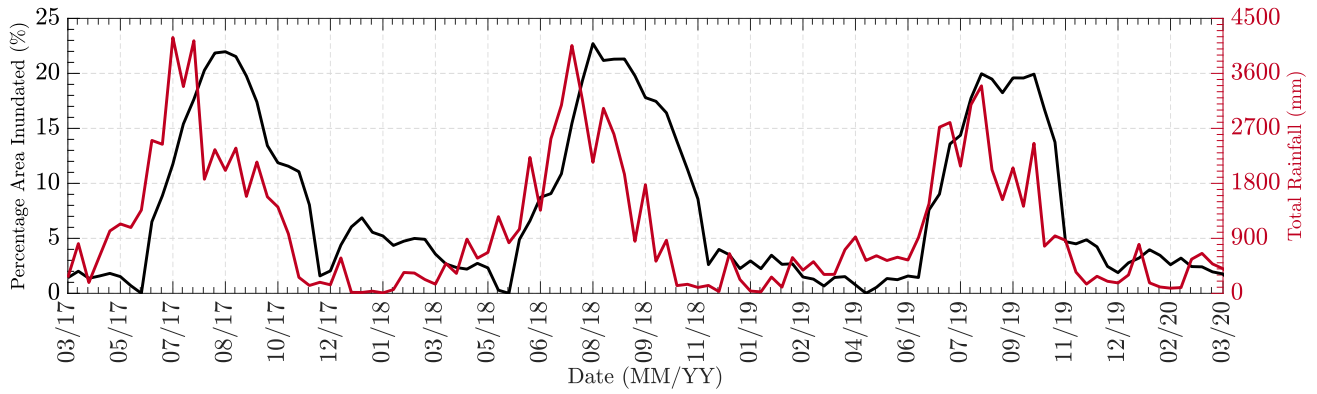


Fig. 5. Case study over India. Detected inundation percentage relative to total area, on 12 km grid using 10 d medians, and total GPM reported rainfall over four dry phases and three wet phases of the monsoon season.

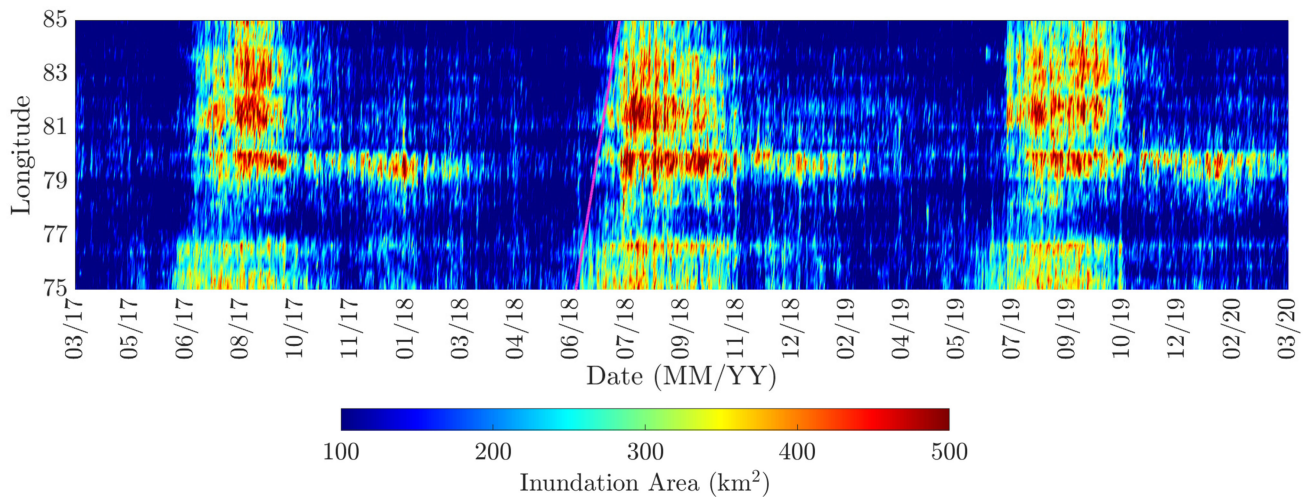


Fig. 6. Hovmöller diagram illustrating areas associated with inundation brought about by the monsoon's wet phase. Trends indicative of the monsoon's dry and wet phases with the slope of the magenta line is used to compute eastward propagation velocity.

determined inundated area is observed. The lag is to be expected, as the proposed mapping methodology detects monsoon dynamics indirectly through its impact on inundation rather than rainfall. During the 2017 wet phase, peak rain occurred on July 20th while peak inundation was detected on August 14th, a lag of 25 d. During 2018 the lag was 21 d. During 2019, however, peak rain and inundation detection coincide on the same day, August 14th. In this case, peak rain is not expected to be the primary driver for the peak in inundation, as peak rainfall in this case was preceded by prolonged periods of above average rainfall throughout India as compared to previous years.

While the results depicted in Figs. 4–5 are indicative of the success of the proposed method in capturing the large scale spatial trends associated with the monsoon's two major phases, dry and wet, their temporal sampling is limited to periods of 1 mo and 10 d, respectively. This is the result of the need to allow a sufficient accumulation of measurements within a given grid cell to investigate the dominance of one mode of scattering over another. Finer spatial grids are therefore inherently associated with coarser temporal resolutions. More frequent temporal

mapping of monsoon dynamics in contrast is possible using coarser spatial grids. To illustrate this, a 25 km grid is used that enables daily updates of coherence estimates and inundation extent.

Fig. 6 illustrates the total daily inundation area obtained over the Indian subcontinent as a function of longitude and time for the three year period March 2017 to March 2020; note the mean area associated with the preceding dry phase is subtracted from the subsequent wet phase to highlight monsoon induced changes. The results clearly illustrate the three wet and four dry phases over this period, as well as the variation of the monsoon's amplitude and duration in longitude. Fig. 7 provides a comparable illustration of the daily GPM rainfall over the same time period and area. The results in Figs. 6 and 7 suggest that the end of the 2017 dry phase was reached, approximately, on June 2nd, 2017. This was followed by a transitional phase that lasted 3 weeks where the Indian subcontinent experienced a combination of transient flooding and inundation. The 2017 transitional dry-wet phase was brought about by rain events in May–June 2017. The wet phase during the same year is found to

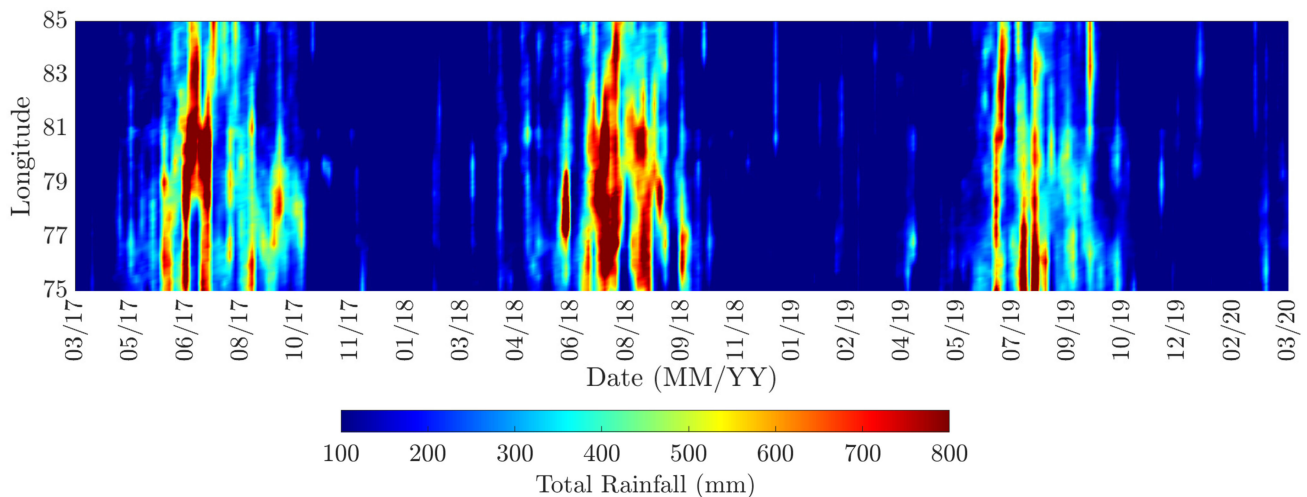


Fig. 7. Hovmöller diagram of GPM derived rain rates illustrating high rain rates characteristic of monsoon's wet phase and low rain rates characteristic of monsoon's dry phase.

range from June 18th, 2017 to September 23rd, 2017, reaching its peak on August 22nd, 2017. A roughly 30 d lag between peak rain, occurring on July 18th, and peak inundation, occurring on August 22nd, is observed. The 2018 wet phase beginning July 8th is found to be delayed by 20 d relative to the previous year. The duration of the three wet phases are also found to undergo variability lasting 98 d in 2017, 85 d in 2018, and 91 d in 2019. The variability in the onset and duration of these phases is indicative of the need for near real time monitoring.

Fig. 6 also shows that the detected inundation undergoes a gradual propagation over the subcontinent, as is evidenced by the lagging onset of comparable levels of inundation along longitude. The 2018 eastward propagation of these effects is marked as an example by the solid line in Fig. 6. In observed propagating speeds are 31.4, 54.9, and 42.4 km/day in 2017, 2018, and 2019, respectively.

V. CONCLUSION

The sensitivity of CYGNSS's land measurements to transient flooding and inundation was used to study the spatial and temporal properties of the South Asian monsoon. To bypass ambiguities and uncertainties associated with relying on DDM magnitudes, a Level-1 coherence detection methodology was specialized to study the monsoon's dry and wet phases. The coherence detection methodology separates DDM measurements into coherent and incoherent categories. Because incoherence is expected to be the dominant mode of scattering over non-inland water surfaces, its persistence over much of the Indian subcontinent is used as an indicator of the monsoon's dry phase. The transition from a mode of incoherence to coherence is used as an indicator of the beginning of the monsoon's wet phase. Comparisons with SMAP soil moistures during the dry and wet phases of the monsoon indicate highly complementary spatial distributions of where inundation is detected. The ability to map the dynamics of the monsoon in near real time with latencies as short as 1 d was illustrated over CYGNSS's multiyear dataset from 2017–2020 and compared to reference GPM precipitation

information. The highly complementary nature of the two further illustrates the ability to use spaceborne GNSS-R systems to support, observe, and predict these large scale cyclical events.

ACKNOWLEDGMENT

The authors would like to thank NASA EOSDIS Physical Oceanography Distributed Active Archive Center (PO.DAAC) at the Jet Propulsion Laboratory, Pasadena, CA for making GNSS-R data derived from the CYGNSS constellation available. They would also like to thank NASA National Snow and Ice Data Center Distributed Active Archive Center (NSIDC.DAAC), Boulder, CO for making radiometer derived data from the SMAP platform available and NASA Goddard Earth Science Data and Information Center (GES DISC) for making GPM derived rain rate data available.

REFERENCES

- [1] P. J. Webster and S. Yang, "Monsoon and ENSO: Selectively interactive systems," *Roy. Meteorological Soc.*, vol. 118, pp. 877–926, 1992.
- [2] B. N. Goswami, *South Asian Monsoon, Intraseasonal Variability of the Atmosphere-Ocean Climate System*, W. K. M. Lau, and D. E. Waliser, Eds., Berlin, Germany: Springer-Verlag, 2005, ch. 2, Art. no. 1961.
- [3] P. J. Webster *et al.*, "Monsoon: Processes, predictability, the prospects for prediction," *J. Geophysical Res.*, vol. 103, pp. 14451–14510, 1998.
- [4] C. Zhang, "Madden-Julian oscillation: Bridging weather and climate," *Bull. Amer. Meteorological Soc.*, vol. 94, no. 12, pp. 1849–1870, 2013.
- [5] E. Douglas *et al.*, "Changes in moisture and energy fluxes due to agricultural land use and irrigation in the Indian monsoon belt," *Geophysical Res. Lett.*, vol. 33, no. 14, 2006.
- [6] World Meteorological Organization, *The Global Climate 2001–2010: A Decade of Climate Extremes Summary Report*, 1st ed. Geneva, Switzerland: WMO, 2013.
- [7] V. Rakesh, R. Singh, and P. Joshi, "Impact of four dimensional assimilation of satellite data on long-range simulations over the Indian region during monsoon 2006," *Adv. Space Res.*, vol. 46, no. 7, pp. 895–908, 2010.
- [8] M. Ramamurthy and F. Carr, "Four-dimensional data assimilation in the monsoon region. Part II: Role of temperature and moisture data," *Monthly Weather Rev.*, vol. 116, no. 10, pp. 1896–1913, 1988.
- [9] R. Singh, C. Kishtawal, S. Ojha, and P. Pal, "Impact of assimilation of atmospheric infraRed sounder (AIRS) radiances and retrievals in the WRF 3D-Var assimilation system," *J. Geophysical Res.*, vol. 117, no. 11, pp. 1–17, 2012.

- [10] C. Ruf *et al.*, "New ocean winds satellite mission to probe hurricanes and tropical convection," *Bull. Amer. Meteorological Soc.*, vol. 97, no. 3, pp. 385–395, 2016.
- [11] C. Ruf *et al.*, "In-Orbit performance of the constellation of CYGNSS hurricane satellites," *Bull. Amer. Meteorological Soc.*, vol. 100, no. 10, pp. 2009–2023, 2019.
- [12] V. U. Zavorotny and A. G. Voronovich, "Scattering of GPS signals from the ocean with wind remote sensing application," *IEEE Trans. Geosci. Remote Sens.*, vol. 38, no. 2, pp. 951–964, Mar. 2000.
- [13] M. M. Al-Khaldi, J. T. Johnson, S. Gleason, E. Loria, A. J. O'Brien, and Y. Yi, "An algorithm for detecting coherence in cyclone global navigation satellite system mission level 1 delay doppler Maps," *IEEE Trans. Geosci. Remote Sens.*, to be published, doi: [10.1109/TGRS.2020.3009784](https://doi.org/10.1109/TGRS.2020.3009784).
- [14] B. Goswami and S. Chakravorty, "Dynamics of the indian summer monsoon climate," *Oxford Res. Encyclopedia Climate Sci.*, 2017. [Online]. Available: [10.1093/acrefore/9780190228620.013.613](https://doi.org/10.1093/acrefore/9780190228620.013.613)
- [15] Q. Wu and Q. Hu, "Atmospheric circulation processes contributing to a multidecadal variation in reconstructed and modeled Indian monsoon precipitation," *J. Geophysical Res.*, vol. 120, no. 2, pp. 532–551, 2015.
- [16] B. Wang *et al.*, "Rethinking Indian monsoon rainfall prediction in the context of recent global warming," *Nat. Commun.*, vol. 6, no. 1, 2015, Art. no. 7154.
- [17] A. Saha, S. Ghosh, A. Sahana, and E. Rao, "Failure of CMIP5 climate models in simulating post-1950 decreasing trend of Indian monsoon," *Geophysical Res. Lett.*, vol. 41, no. 20, pp. 7323–7330, 2014.
- [18] S. Gleason, C. Ruf, M. Clarizia, and A. O'Brien, "Calibration and unwrapping of the normalized scattering cross section for the cyclone global navigation satellite system," *IEEE Trans. Geosci. Remote Sens.*, vol. 54, no. 5, pp. 2495–2509, May 2016.
- [19] T. Antony, C. S. Raju, N. Mathew, and K. K. Moorthy, "Flood extent analysis over the major river basins in the indian subcontinent using satellite microwave radiometric data," *IEEE J. Sel. Top. Appl. Earth Observ. Remote Sens.*, vol. 8, no. 9, pp. 4373–4378, 2015.
- [20] F. Papa, C. Prigent, F. Durand, and W. Rossow, "Wetland dynamics using a suite of satellite observations: A case study of application and evaluation for the Indian Subcontinent," *Geophysical Res. Lett.*, vol. 33, no. 8, 2006.
- [21] N. Pierdicca, L. Pulvirenti, M. Chini, L. Guerriero, and L. Candela, "Observing floods from space: Experience gained from COSMO-SkyMed observations," *Acta Astronautica*, vol. 84, pp. 122–133, 2013.
- [22] R. Hoque, D. Nakayama, H. Matsuyama, and J. Matsumoto, "Flood monitoring, mapping and assessing capabilities using RADARSAT remote sensing, GIS and ground data for Bangladesh," *Natural Hazards*, vol. 57, no. 2, pp. 525–548, 2010.
- [23] J. Sanyal and X. Lu, "Application of remote sensing in flood management with special reference to monsoon Asia: A Review," *Natural Hazards*, vol. 33, no. 2, pp. 283–301, 2004.
- [24] J. Ouellette *et al.*, "A Time-series approach to estimating soil moisture from vegetated surfaces using l-band radar backscatter," *IEEE Trans. Geosci. Remote Sens.*, vol. 55, no. 6, pp. 3186–3193, Jun. 2017.
- [25] L. Pulvirenti, M. Chini, N. Pierdicca, and G. Boni, "Use of SAR data for detecting floodwater in urban and agricultural areas: The role of the interferometric coherence," *IEEE Trans. Geosci. Remote Sens.*, vol. 54, no. 3, pp. 1532–1544, Mar. 2016.
- [26] A. G. Voronovich and V. U. Zavorotny, "Bistatic radar equation for signals of opportunity revisited," *IEEE Trans. Geosci. Remote Sens.*, vol. 56, no. 3, pp. 1959–1968, Apr. 2018.
- [27] A. Balakhder, M. Al-Khaldi, and J. Johnson, "On the coherency of ocean and land surface specular scattering for GNSS-R and signals of opportunity systems," *IEEE Trans. Geosci. Remote Sens.*, vol. 57, no. 12, pp. 10426–10436, Dec. 2019.
- [28] M. Al-Khaldi, J. Johnson, A. O'Brien, A. Balenzano, and F. Mattia, "Time-series retrieval of soil moisture using CYGNSS," *IEEE Trans. Geosci. Remote Sens.*, vol. 57, no. 7, pp. 4322–4331, Jul. 2019.
- [29] A. Mialon *et al.*, "Comparison of Dobson and Mironov dielectric models in the SMOS soil moisture retrieval algorithm," *IEEE Trans. Geosci. Remote Sens.*, vol. 53, no. 6, pp. 3084–3094, Jun. 2015.
- [30] C. Chew, J. Reager, and E. Small, "CYGNSS data map flood inundation during the 2017 Atlantic hurricane season," *Sci. Rep.*, vol. 8, no. 1, 2018.
- [31] M. Morris, C. Chew, J. T. Reager, R. Shah, and C. Zuffada, "A novel approach to monitoring wetland dynamics using CYGNSS: Everglades case study," *Remote Sens. Environ.*, vol. 233, Nov. 2019.
- [32] C. Gerlein-Safdi and C. Ruf, "A CYGNSS based algorithm for the detection of Inland waterbodies," *Geophysical Res. Lett.*, vol. 46, no. 21, pp. 12065–12072, Nov. 2019.
- [33] N. Rodríguez-Alvarez, E. Podest, K. Jensen, and K. McDonald, "Classifying inundation in a tropical wetlands complex with GNSS-R," *Remote Sens.*, vol. 11, no. 9, 2019, Art. no. 1053.
- [34] K. Jensen, K. McDonald, E. Podest, N. Rodríguez-Alvarez, V. Horna, and N. Steiner, "Assessing L-Band GNSS-Reflectometry and imaging radar for detecting Sub-canopy inundation dynamics in a tropical wetlands complex," *Remote Sens.*, vol. 10, no. 9, 2018, Art. no. 1431.
- [35] H. Carreno-Luengo, G. Luzi, and M. Crosetto, "Sensitivity of CyGNSS bistatic reflectivity and SMAP microwave radiometry brightness temperature to geophysical parameters over land surfaces," *IEEE J. Sel. Top. Appl. Earth Observ. Remote Sens.*, vol. 12, no. 1, pp. 107–122, 2019.
- [36] M. M. Al-Khaldi *et al.*, "Inland water body mapping using CYGNSS coherence detection," *IEEE Trans. Geosci. Remote Sens.*, to be published, doi: [10.1029/2019GL085134](https://doi.org/10.1029/2019GL085134).
- [37] A. Egido *et al.*, "Airborne GNSS-R polarimetric measurements for soil moisture and above-ground biomass estimation," *IEEE J. Sel. Top. Appl. Earth Observ. Remote Sens.*, vol. 7, no. 5, pp. 1522–1532, 2014.
- [38] S. Gleason, C. Ruf, A. O'Brien, and D. McKague, "The CYGNSS level 1 calibration algorithm and error analysis based on on-orbit measurements," *IEEE J. Sel. Top. Appl. Earth Observ. Remote Sens.*, pp. 1–13, 2018.
- [39] T. Wang, C. Ruf, B. Block, D. McKague, and S. Gleason, "Design and performance of a GPS constellation power monitor system for improved CYGNSS L1B calibration," *IEEE J. Sel. Top. Appl. Earth Observ. Remote Sens.*, vol. 12, no. 1, pp. 26–36, 2019.
- [40] S. Chan, E. Njoku, and A. Colliander, "Soil moisture active passive: Algorithm theoretical basis document (ATBD) for level 1C radiometer data product," Jet Propulsion Laboratory, Pasadena, CA, USA, 2014.
- [41] M. Rahman *et al.*, "Agriculture flood mapping with soil moisture active passive (SMAP) data: A case of 2016 Louisiana flood," in *Proc. 6th Int. Conf. Agro-Geoinformatics*, 2017, doi: [10.1109/Agro-Geoinformatics.2017.8047062](https://doi.org/10.1109/Agro-Geoinformatics.2017.8047062).
- [42] H. Fujisada, M. Urai, and A. Iwasaki, "Technical methodology for ASTER global water body data base," *Remote Sens.*, vol. 10, no. 12, 2018, Art. no. 1860. [Online]. Available: [10.3390/rs10121860](https://doi.org/10.3390/rs10121860)
- [43] J. Pekel, A. Cottam, N. Gorelick, and A. Belward, "High-resolution mapping of global surface water and its long-term changes," *Nature*, vol. 540, no. 7633, pp. 418–422, 2016.
- [44] T. Iguchi *et al.*, "GPM/DPR level-2 algorithm theoretical basis document," NASA Goddard Space Flight Center, Greenbelt, MD, USA, Tech. Rep., 2010.
- [45] S. Gleason, A. O'Brien, A. Russel, M. M. Al-Khaldi, and J. T. Johnson, "Geolocation, calibration and surface resolution of spaceborne GNSS-R land observations," *Remote Sens.*, vol. 12, no. 8, 2020.



Mohammad M. Al-Khaldi (Member, IEEE) received the bachelor's degree in electrical engineering from the American University of Sharjah, Sharjah, United Arab Emirates, in 2015, the M.S. degree in electrical engineering from Texas A&M University, College Station, TX, USA, in 2017, the M.S. and Ph.D. degrees in electrical and computer engineering from The Ohio State University, Columbus, OH, USA, in 2019 and 2020, respectively.

He is currently a Postdoctoral Researcher with the Constellation Observing System for Meteorology, Ionosphere, and Climate Program (COSMIC), University Corporation for Atmospheric Research (UCAR). His research interests include applied electromagnetics, rough surface scattering, and spaceborne remote sensing.



Rashmi Shah (Senior Member, IEEE) received the M.S. degree in engineering and the Ph.D. degree in aeronautics and astronautics from Purdue University, West Lafayette, IN, USA, in 2010 and 2014, respectively. Her research was on remote sensing using digital communication signals of opportunity.

Since 2014, she has been a Research Technologist with NASA Jet Propulsion Laboratory, Pasadena, CA, USA, where she is leading signals of opportunity effort. Her research interests include the use of satellite digital communication signals as a source of opportunity for remote sensing applications.



Clara C. Chew (Member, IEEE) received the B.A. degree in environmental studies from Dartmouth College, Hanover, NH, USA, in 2009, and Ph.D. in geological sciences from the University of Colorado, Boulder, CO, USA, in 2015.

She is currently a project scientist with the University Corporation for Atmospheric Research, Boulder, CO, USA. Her research interests are centered around using remote sensing data to monitor the terrestrial hydrologic cycle.



Joel T. Johnson (Fellow, IEEE) received the bachelor's degree in electrical engineering degree from the Georgia Institute of Technology, Atlanta, GA, USA, in 1991, and the S.M. and Ph.D. degrees from the Massachusetts Institute of Technology, Cambridge, MA, USA, in 1993 and 1996, respectively.

He is currently a Professor with the ElectroScience Laboratory, Department of Electrical and Computer Engineering, The Ohio State University, Columbus, OH, USA. His current research interests include the areas of microwave remote sensing, propagation, and

electromagnetic wave theory.

Dr. Johnson is a member of commissions B and F of the International Union of Radio Science (URSI), Tau Beta Pi, Eta Kappa Nu, and Phi Kappa Phi. He received the 1993 Best Paper Award from the IEEE Geoscience and Remote Sensing Society, was named an Office of Naval Research Young Investigator, National Science Foundation Career Awardee, PECASE Award Recipient in 1997, and was recognized by the U.S. National Committee of URSI as a Booker Fellow, in 2002. He served as Technical Program Co-Chair for the 2017 International Geoscience and Remote Sensing Symposium. He has served as an Associate Editor for the *TRANSACTIONS ON GEOSCIENCE AND REMOTE SENSING*, since 2000. He is also a Past Chair of the GRSS Technical Committee on Frequency Allocations in Remote Sensing.



Scott Gleason (Senior Member, IEEE) received the B.S. degree in electrical and computer engineering from the State University of New York at Buffalo, Buffalo, NY, USA, the M.S. degree in engineering from Stanford University, Stanford, CA, USA, and the Ph.D. degree in applied physics from the University of Surrey, Surrey, U.K., 1991, 1999, and 2007, respectively.

He is a Project Scientist III with the University Corporation for Atmospheric Research, Boulder, CO, USA. He is a Co-Investigator on the science team and Instrument Scientist for the NASA CYGNSS mission. He has worked in the areas of astronautics, remote sensing, and global navigation satellite systems for more than 20 years, including at NASAs Goddard Space Flight Center, Stanfords GPS Laboratory, Surrey Satellite Technology Limited, Concordia University, and the National Oceanography Centre, Southampton.